



## Preparation of mesoporous graphene oxide/SBA-15 hybrid nanoparticles as a potential adsorbent for removal of cationic dyes

Tzong-Horng Liou<sup>a,b,\*</sup>, Ming-Hui Lin<sup>a</sup>

<sup>a</sup>Department of Chemical Engineering, Ming Chi University of Technology, 84 Gungjuan Rd., Taishan, New Taipei 24301, Taiwan, Tel. +886-2-29089899 Ext. 4617; Fax: +886-2-29083072; emails: thliou@mail.mcut.edu.tw (T.-H. Liou), lin19911201@gmail.com (M.-H. Lin)

<sup>b</sup>Battery Research Center of Green Energy, Ming Chi University of Technology, 84 Gungjuan Rd., Taishan, New Taipei 24301, Taiwan

Received 30 October 2018; Accepted 1 March 2019

### ABSTRACT

In this paper, mesoporous graphene oxide/SBA-15 nanocomposite was used as an adsorbent for removing cationic dyes from wastewater. Adsorption experiments tested the initial concentration of dye, calcination temperature, and pH of dye solution. The features of the composite were examined through X-ray diffractometry, field-emission scanning electron microscopy, transmission electron microscopy, Raman spectrometry, Fourier transform infrared spectrometer, and surface area analysis. The graphene oxide/SBA-15 samples possessed a high degree of oxidation that gave the composite an excellent adsorptive property toward dye. Higher solution pH and initial concentration of dye favored methylene blue adsorption. Adsorption capacity was highest at a calcination temperature of 550°C. Adsorption kinetics and isotherms were analyzed. The adsorption process was well fitted by the pseudo-second order kinetic model and Langmuir isotherm model. The mesoporous graphene oxide/SBA-15 composite is a promising material for removing aqueous organic pollutants.

*Keywords:* Graphene oxide; SBA-15; Mesostructure; Nanocomposite; Cationic dye

### 1. Introduction

Graphene possesses a single layer of two-dimensional sp<sup>2</sup>-bonded carbon atoms arranged in a hexagonal form. The carbon material has excellent electrochemical, optical, and mechanical properties, which make it an ideal candidate for applications in biomedical [1], batteries [2], sensors [3], photocatalysts [4], nanocomposites [5], and supercapacitors [6]. Graphene oxide (GO) possesses numerous oxygen atoms on the surface in the form of epoxy, hydroxyl, and carboxyl groups [7]. Because of its large specific surface area and abundant oxygen-containing functional groups, GO has been suggested as an effective adsorbent to remove organic and inorganic pollutants [8–11]. With increasing application of GO in wastewater treatment, some disadvantages restrict its practical application for dye removal. For example,

powdered GO is hydrophilic, and water soluble; thus, it is difficult to filter and reuse [12]. Different types of support materials, including zeolites [13], mesoporous silica nanoparticles [14], activated carbons [15], carbon nanotubes [16,17], and biomaterials such as chitosan [18], high gluten flour [19] and corn zein [20], are the most popular research objects because of their high surface areas and dispersible efficiency. Among these support materials, SBA-15 has been identified as a mesoporous silica material with an amorphous phase. The silica material shows high mechanical strength and thermal stability as well as uniform porosity. Moreover, SBA-15 possesses large surface area (600–1,000 m<sup>2</sup> g<sup>-1</sup>), large pore volume (0.8–2.0 cm<sup>3</sup> g<sup>-1</sup>), adjustable pore size (5–30 nm), and thick silica wall (3–6 nm) [21]. The large surface area of SBA-15 can provide abundant adsorption sites and plays a crucial role in increasing the adsorption efficiency and reuse of GO.

\* Corresponding author.

Worldwide dye production is over 1,00,000 tons each year [22]. Methylene blue (MB) is used as a coloring agent in aquaculture and in calico, cotton, and leather products [23]. The dye wastewater produced from many industries is undesirable. These dyes have aromatic rings in their structures, which have various harmful effects on humans and animals because of their high toxicity, non-biodegradability, carcinogenicity, and mutagenicity [24]. Various treatment techniques have been employed to remove dyes, such as adsorption, coagulation or flocculation, ion-exchange, membrane filtration, photocatalytic degradation, and solvent extraction [25,26]. Adsorption is the most widely used of these for its simplicity of operation and design, low cost, and effectiveness at removing dyes in low concentrations. Therefore, adsorption has become a favored choice for removing MB.

Numerous studies have reported adsorption of dyes onto GO or reduced-GO materials. However, few studies have focused on GO-based hybrid materials as potential adsorbents. Wu et al. [14] reported that Fe<sub>3</sub>O<sub>4</sub>-graphene/silica nanocomposites were prepared by decoration of Fe<sub>3</sub>O<sub>4</sub> nanoparticles onto graphene sheets stepped by the deposition of a layer of mesoporous SiO<sub>2</sub> onto the surface. The adsorption capacity of the nanocomposite was highly dependent on pH and temperature. Wanjeri et al. [27] investigated the adsorption of organophosphorus pesticides on GO-based silica coated magnetic nanoparticles functionalized with 2-phenylethylamine. The heterogeneity of the adsorption process was attributed to the various surface groups on the nanocomposite, and the resulting hydrogen bonding and  $\pi$ - $\pi$  interaction between the nanocomposite and the electronegative atoms (P, N, and S) on the pesticides. Wang et al. [28] fabricated graphene aerogels/mesoporous silica through electrostatic interaction between negatively charged GO and cationic surfactant and self-assembly of surfactant. The mesoporous silica was nucleated homogeneously and grown on the surface of graphene aerogels. The composite showed superior capacity for removal of phenols from wastewater. Du et al. [24] used a wet spinning technique to prepare GO/chitosan/silica fibers. Silica nanoparticles were subsequently etched off to produce porous GO/chitosan composites. They found that acidic conditions benefited congo red adsorption, and the adsorption capacity reached 123.7 mg g<sup>-1</sup> at pH 3.0.

In this work, preparation of GO/SBA-15 nanocomposite and its efficacy for removing MB from aqueous solution are reported. The GO was grafted onto the surface of the SBA-15. The effects of the initial concentration of dye, calcination temperature, and pH of solution on MB adsorption were systematically studied. This investigation characterized GO/SBA-15 materials through transmission electron microscopy (TEM), field-emission scanning electron microscopy (FESEM), X-ray diffractometry (XRD), surface area analysis, and Raman spectrometry. Additionally, adsorption kinetics and isotherms were analyzed in detail.

## 2. Experimental setup

### 2.1. Materials

Reagents with high purity were used to prepare the nanocomposite, including tetraethyl orthosilicate (TEOS, Sigma-Aldrich), pluronic triblock copolymer (P123, Sigma-Aldrich), MB (C<sub>16</sub>H<sub>18</sub>ClN<sub>3</sub>S, Acros Organics), graphite powder

(Sigma-Aldrich), sodium nitrate (NaNO<sub>3</sub>, Acros Organics), hydrogen peroxide (H<sub>2</sub>O<sub>2</sub>, Acros Organics), potassium permanganate (KMnO<sub>4</sub>, Acros Organics), hydrochloric acid (HCl, Merck), sulfuric acid (H<sub>2</sub>SO<sub>4</sub>, Merck), sodium hydroxide (NaOH, Merck), nitrogen and air (Sun Fu Co., 99.995%). All materials used in this study were analytical grade and used as received without further purification.

### 2.2. Synthesis of GO

The GO was synthesized from graphite powder according to a modified Hummers method [29,30]. A mixture of graphite powder, NaNO<sub>3</sub> and H<sub>2</sub>SO<sub>4</sub> was blended together in a flask under constant stirring. Subsequently, KMnO<sub>4</sub> was added slowly to the reaction in an ice-water bath under vigorous agitation. Then, the mixture was maintained at 30°C–40°C for 2 h with continuous stirring. After mixing, water was added through stirring. Subsequently, H<sub>2</sub>O<sub>2</sub> was added slowly into the mixture. The solid mixture was rinsed with diluted HCl solution and dried in air oven. Finally, the GO solution was obtained by dispersing the solid into water through ultrasonication.

### 2.3. Synthesis of mesoporous GO/SBA-15

The mesoporous GO/SBA-15 nanocomposites were synthesized using a hydrothermal method. A total of 6.0 g of 1.0 wt% GO solution, 4.0 g P123, and 1.0 M H<sub>2</sub>SO<sub>4</sub> were dissolved in 120 mL of aqueous solution by stirring at 40°C. Thereafter, 9.2 mL of TEOS was slowly added to the surfactant solution. After stirring for 20 h, the mixture was placed into a 100 mL Teflon-lined autoclave and maintained at 100°C for 24 h. After cooling, the obtained solids were separated using a high-speed centrifuge and washed with distilled water. The samples were then filtered and dried to remove water. The GO/SBA-15 products were finally obtained through thermal treatment of the as-synthesized sample at 550°C for 6 h in a tubular furnace with nitrogen gas.

For the purpose of comparison, pure SBA-15 was synthesized from P123 surfactant and TEOS using the same process of titration, hydrothermal treatment, water-washing, and calcination, except for the addition of GO solution.

### 2.4. Adsorption experiment of GO/SBA-15

Batch adsorption experiments were conducted by adding 50 mg of GO/SBA-15 to 250 mL of MB aqueous solution with various concentrations (10–50 mg L<sup>-1</sup>). The suspensions were stirred continuously at room temperature. The experiments concerning about the effects of solution pH and calcination temperature on adsorption capacity were conducted through a series of tests with initial pH of MB ranging from 3 to 11 and calcination temperatures from 350°C to 750°C. The suspensions were collected at fixed time intervals and subsequently filtered through centrifugation and a membrane filter. The MB concentrations before and after adsorption were determined using a UV-vis Genesys spectrophotometer (Thermo Electron Corporation) at a maximum adsorption wavelength of 665 nm. The MB uptake was calculated using the following equation:

$$q_t = \frac{(C_o - C_t)V}{W} \quad (1)$$

where  $q_t$  ( $\text{mg g}^{-1}$ ) is the amount of MB adsorbed onto the GO/SBA-15;  $C_0$  and  $C_t$  ( $\text{mg L}^{-1}$ ) are the initial MB concentration and the concentration at different adsorption times, respectively;  $V$  (mL) denotes the volume of the solution; and  $W$  (g) is the weight of the GO/SBA-15.

Reutilization experiments were performed by using high purity (99.0%) ethanol as desorption agent. GO/SBA-15 samples were mixed with MB solution at room temperature. After reaching adsorption equilibrium, the solid samples were collected and were repeatedly washed with the ethanol solution. Then, the solids were washed with distilled water to remove the ethanol. The regenerated samples were moved to air oven before secondary adsorption. The adsorption-desorption process was repeated five times.

### 2.5. Characterization of adsorbent samples

The  $\text{N}_2$  adsorption-desorption isotherm was determined to obtain the specific surface area, pore volume, and pore size distribution using a Micrometric ASAP 2010 surface area and porosity analyzer. The specific surface area and pore size of the samples were calculated using the Brunauer–Emmett–Teller (BET) and Barrett–Joyner–Halenda (BJH) methods, respectively [31]. The total pore volume was determined on the basis of the volume of adsorbed nitrogen at a relative pressure of 0.99. The mesophase (low-angle) and crystalline structure (wide-angle) of the GO and GO/SBA-15 samples were recorded using a powder X-ray diffractometer (PANalytical, model X'pert pro system) with  $\text{Cu-K}\alpha$  radiation.

The surface morphology of GO/SBA-15 was analyzed using a JSM-6700F (JEOL) field-emission scanning electron microscope. The pore structure of the synthesized GO/SBA-15 samples was identified through TEM (JEM-1200CX II, JEOL). Raman spectra were obtained from a confocal micro-Renishaw with 632 nm He-Ne laser excitation. The Fourier transform infrared spectrum of sample was characterized using a Shimadzu FTIR-8300 spectrometry.

## 3. Results and discussion

### 3.1. Adsorption of MB on SBA-15 and GO/SBA-15 materials

Fig. 1 shows that the adsorption capacity of SBA-15 and GO/SBA-15 increased with increasing adsorption time. The SBA-15 sample exhibited a longer time to reach adsorption equilibrium than did the GO/SBA-15 composite. Moreover, the GO/SBA-15 sample exhibited a higher capacity for removing MB than did pure SBA-15. The addition of GO enhanced the adsorption capacity of the nanocomposite; this can be attributed to its high surface area and the strong  $\pi$ - $\pi$  interactions with the MB molecules [32].

The effect of the initial concentration of MB on the adsorption capacity of GO/SBA-15 is presented in Fig. 2. The adsorption rate increased rapidly with initial adsorption duration. The observation indicates that numerous vacant surface sites were available for MB adsorption. However, the adsorption rate slowed when nearing equilibrium because it was difficult to occupy the remaining vacant sites. The experimental results also showed that the higher the initial concentration was, the higher the MB uptake became. The amount of MB adsorption at equilibrium increased from 58 to 159  $\text{mg g}^{-1}$

as the initial concentration increased from 10 to 50  $\text{mg L}^{-1}$ . Increasing the initial concentration of MB increased the MB around the adsorbent, enhancing the adsorption amount of MB. A similar observation of MB adsorption on zeolite bio-composite was reported elsewhere [33].

Fig. 3 shows that changes in the sample's calcination temperature markedly influenced MB adsorption. The adsorption capacity was lowest ( $95 \text{ mg g}^{-1}$ ) at a calcination temperature of  $350^\circ\text{C}$  and highest ( $138 \text{ mg g}^{-1}$ ) at a calcination temperature of  $550^\circ\text{C}$ , at which the GO/SBA-15 sample possessed the highest surface area. Likewise, the lowest surface area was observed at a calcination temperature of  $350^\circ\text{C}$ . Surface area analysis presented in a later section. Under normal circumstances, increasing the adsorbent's surface area increased the activity sites for the adsorption of the adsorbate. The results

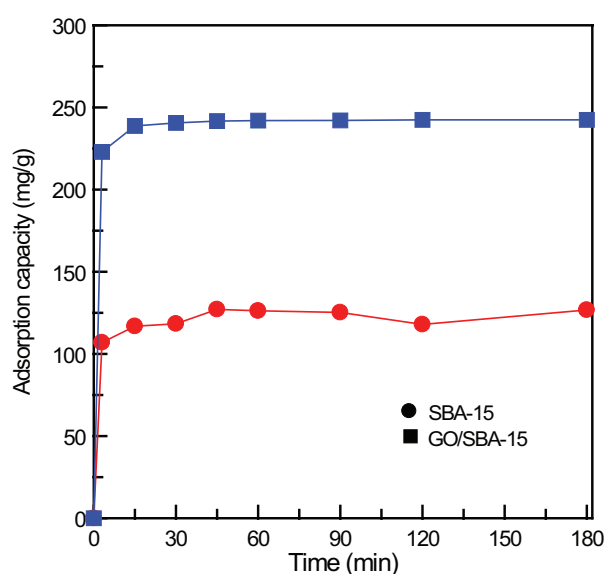


Fig. 1. Adsorption of MB onto GO/SBA-15 and pure SBA-15.

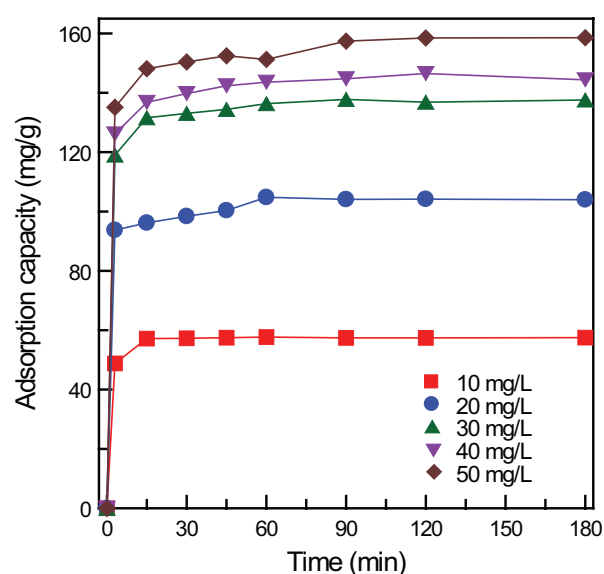


Fig. 2. Effect of initial concentration on MB adsorption onto GO/SBA-15.

demonstrated an enhanced removal rate of MB. The adsorption capacities of samples at various calcination temperatures were, in order,  $550^{\circ}\text{C} > 750^{\circ}\text{C} > 650^{\circ}\text{C} > 450^{\circ}\text{C} > 350^{\circ}\text{C}$ .

The pH value is an influential parameter in the adsorption process. Fig. 4 shows the effects of solution pH on MB adsorption onto GO/SBA-15 in the pH range of 3–11. The MB adsorption on GO/SBA-15 was highly dependent on solution pH. In this study, the highest adsorption capacity of  $258 \text{ mg g}^{-1}$  was recorded at pH 11. The lowest adsorption capacity of  $56 \text{ mg g}^{-1}$  was recorded at pH 3. MB ions are those of a cationic dye. An increase in  $\text{OH}^-$  at high pH enhances

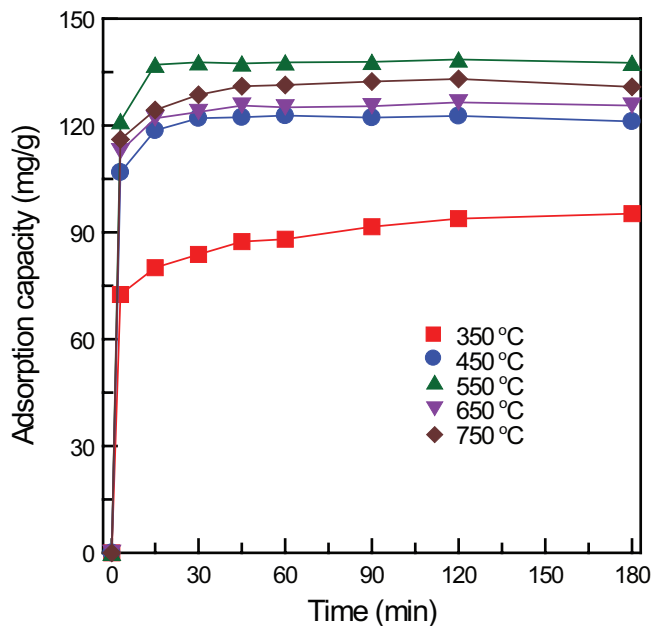


Fig. 3. Effect of calcination temperature on MB adsorption onto GO/SBA-15.

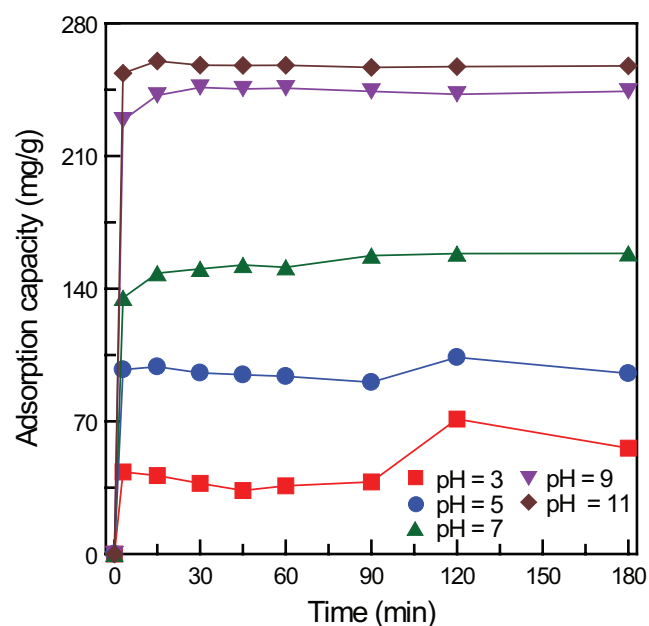


Fig. 4. Effect of solution pH on MB adsorption onto GO/SBA-15.

MB adsorption capacity. Highly acidic conditions are unfavorable for MB adsorption. It may be that the excess  $\text{H}^+$  ions present competed with the MB ions for adsorption sites. Thus, the adsorption of MB decreased. [34]. Additionally, the solution pH may change the surface charge on the adsorbent. In a basic solution, the electrostatic attraction between the negatively charged GO/SBA-15 surface and cationic MB dye molecules results in higher MB adsorption than in an acidic solution. Wu et al. [14] investigated the adsorption capacity of MB onto  $\text{Fe}_3\text{O}_4$ -graphene/ $\text{SiO}_2$  composites and observed that increasing pH increased the adsorption of MB. This observation is consistent with our experimental results.

### 3.2. Pore structure analysis

As shown in Fig. 5(a) the nitrogen adsorption-desorption measurements for GO/SBA-15 samples at calcination temperatures between  $350^{\circ}\text{C}$  and  $750^{\circ}\text{C}$  were performed at 77 K to investigate the sample's pore characteristics. All isotherms

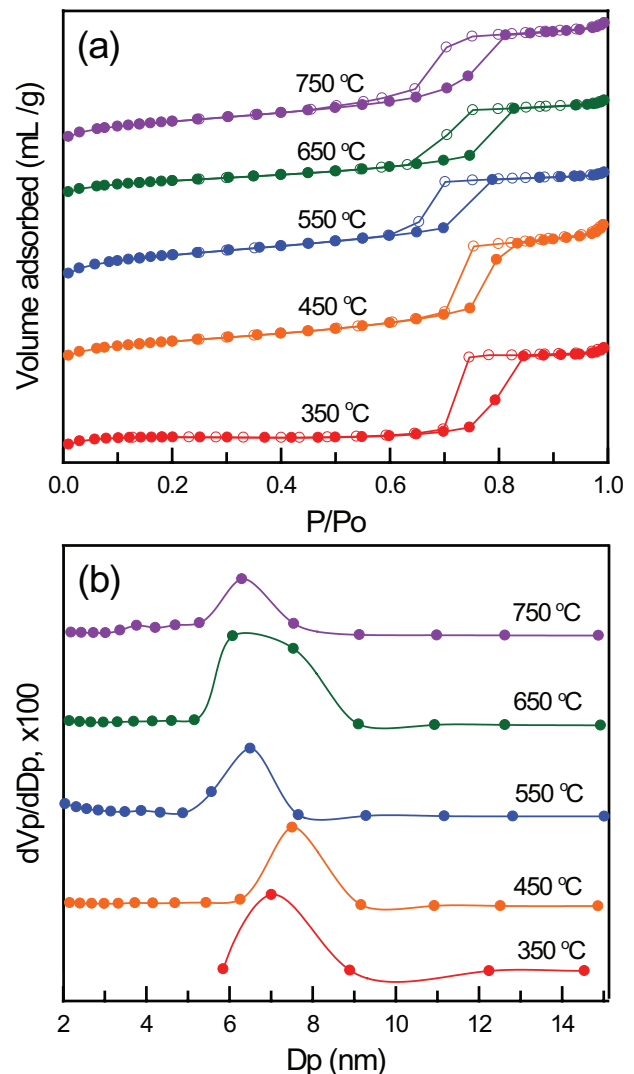


Fig. 5. (a) Nitrogen adsorption-desorption isotherm and (b) differential pore size distribution of GO/SBA-15 samples at various calcination temperatures.

were type IV with an H1 hysteresis loop at  $P/P_0 = 0.6$ – $0.9$  according to International Union of Pure and Applied Chemistry (IUPAC) classification, which indicated that the synthesized materials were mesoporous in structure [35]. Comparison of the GO/SBA-15 samples prepared at various calcination temperatures revealed that the isotherms were similar. This observation indicates that the addition of GO into SBA-15 does not affect the mesostructure of the SBA-15 framework. As illustrated in Fig. 5(b) the pore diameters of GO/SBA-15 composites were 6.08–7.51 nm. The pore sizes of samples exhibited a uniform and narrow distribution. This observation indicates that the pore framework of GO/SBA-15 is highly stable. Composites obtained at calcination temperatures of 350°C–450°C had higher pore diameters than those at calcination temperatures of 550°C–750°C. Table 1 shows the specific surface area, pore volume, and pore diameter of adsorbent samples. The GO/SBA-15 at a calcination temperature of 350°C had the lowest specific surface area ( $477 \text{ m}^2 \text{ g}^{-1}$ ) and pore volume ( $0.936 \text{ cm}^3 \text{ g}^{-1}$ ). Surfactants were likely not completely removed and caused a pore obstruction in the SBA-15 framework. GO/SBA-15 at a calcination temperature of 550°C possessed the highest specific surface area of  $891 \text{ m}^2 \text{ g}^{-1}$  and large pore volume of  $1.035 \text{ cm}^3 \text{ g}^{-1}$ . The decreased specific surface area at calcination temperatures of 650°C ( $669 \text{ m}^2 \text{ g}^{-1}$ ) and 750°C ( $683 \text{ m}^2 \text{ g}^{-1}$ ) can be attributed to the violent gasification reactions that destroyed part of the pore structure [36].

Most microporous adsorbents are highly efficient at removing low-molecular-weight compounds. However, high-molecular-weight dyes (e.g., MB) have difficulty entering the micropores. GO/SBA-15 has a well-developed mesopore structure, which is beneficial for removing MB molecules.

### 3.3. Analysis of sample composition and phase characteristics

Fig. 6(a) shows the mesoporous phase characteristics of pure SBA-15 and GO/SBA-15 samples obtained through low-angle XRD. The two samples showed XRD patterns corresponding to (100), (110), and (200) reflections, characteristics of SBA-15 with a hexagonally ordered mesoporous structure [37]. The XRD patterns of the pure SBA-15 and GO/SBA-15 were similar. This suggests that the mesostructure of the SBA-15 sample was unaffected by the addition of GO. Fig. 6(b) shows a wide range scan of XRD patterns of the GO sample with  $2\theta$  values ranging from  $10^\circ$  to  $70^\circ$ . The sample showed an intense diffraction peak centered at a  $2\theta$  angle of near  $10^\circ$ ,

a characteristic of GO powder in (200) plane reflection. This observation indicated that GO was successfully synthesized from the graphite powder. During the oxidation process, the regular crystalline structure of the starting graphite was damaged, and the oxygenous functional groups were formed [38].

Fig. 7(a) illustrates the Raman spectra of GO/SBA-15 composites synthesized at various calcination temperatures. There were two intensive D and G peaks at  $1,330$  and  $1,600 \text{ cm}^{-1}$ , respectively. These spectra indicate that calcination temperature can influence the order and degree of graphitization of GO/SBA-15 samples. The G-band was assigned to  $\text{sp}^2$  carbon atoms, and the D-band corresponded to structural defects from disorder vacancies and functional groups [39]. A narrow and intense G band indicated the formation of graphitic domains. The intensity ratios of the D and G bands ( $I_D/I_G$ ) were  $0.864$ – $0.957$  (Table 2). The ratio decreased with increasing calcination temperature from  $350^\circ\text{C}$  to  $650^\circ\text{C}$ . This observation indicated that majority of samples underwent a high degree of oxidation [40]. The FTIR spectrum of GO/SBA-15 sample is presented in Fig. 7(b). The spectrum corresponded to a variety of functional groups such as OH ( $\sim 3,500 \text{ cm}^{-1}$ ), C=O ( $\sim 1,635 \text{ cm}^{-1}$ ), C=C ( $\sim 1,605 \text{ cm}^{-1}$ ),  $-\text{CH}_3$  ( $\sim 1,375 \text{ cm}^{-1}$ ), Si-OH ( $\sim 980 \text{ cm}^{-1}$ ) and Si-O-Si ( $\sim 790$  and  $450 \text{ cm}^{-1}$ ). The FTIR spectrum confirmed that the GO/SBA-15 contained different oxygen functional groups: hydroxyl, carbonyl, and carboxylic groups [7]. The presence of oxygen groups had a higher negative potential, which was favorable for the adsorption of cationic dyes (MB) to form a dye complex.

### 3.4. Surface morphology of GO/SBA-15 samples

SEM images of the GO/SBA-15 samples synthesized at various calcination temperatures are illustrated in

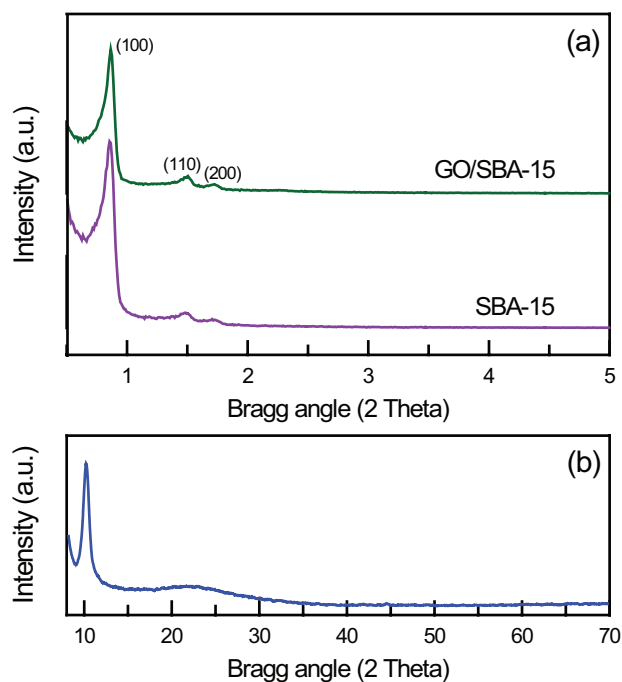


Fig. 6. X-ray diffraction patterns: (a) low-angle spectra of GO/SBA-15 and pure SBA-15, and (b) wide-angle spectrum of pure GO.

Table 1  
Surface area, pore volume and pore diameter of adsorbent samples at various calcination temperatures

Temperature ( $^\circ\text{C}$ )	$S_{\text{BET}}$ ( $\text{m}^2 \text{ g}^{-1}$ )	$V_t$ ( $\text{cm}^3 \text{ g}^{-1}$ )	$d_p$ (nm)
350	477	0.936	7.01
450	745	1.543	7.51
550	891	1.035	6.50
650	669	1.276	6.08
750	683	1.169	6.30

$S_{\text{BET}}$  = specific surface area,  $V_t$  = total pore volume,  $d_p$  = pore diameter (BJH desorption).

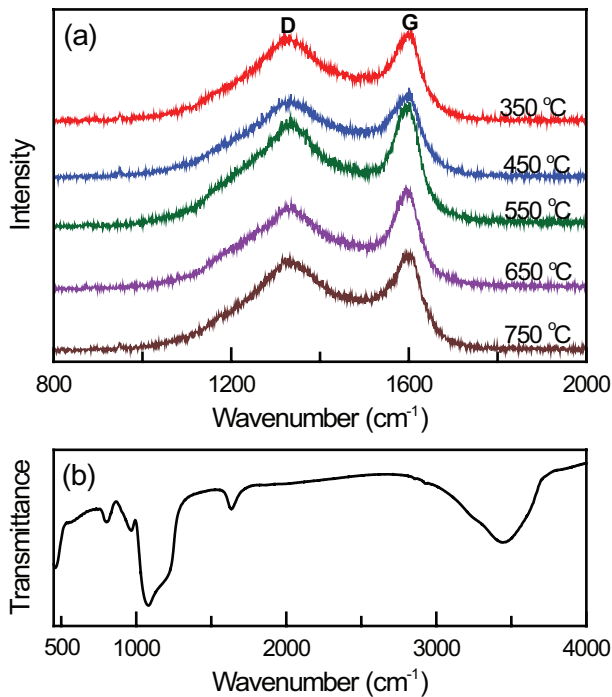


Fig. 7. (a) Raman spectra of GO/SBA-15 at various calcination temperatures, and (b) FTIR spectrum of GO/SBA-15.

Table 2

Intensity of D band and G band of Raman spectra for adsorbent samples at various calcination temperatures

Temperature (°C)	$I_{D\text{-band}}$	$I_{G\text{-band}}$	$A (I_D/I_G)$
350	1,378.36	1,440.86	0.957
450	1,343.98	1,436.72	0.935
550	1,834.13	2,046.29	0.896
650	1,417.35	1,639.51	0.864
750	1,462.77	1,530.70	0.956

Fig. 8. Fig. 8(a) shows the surface morphology of GO/SBA-15 obtained at a calcination temperature of 350°C. The particles were of micrometer size with a relatively rough surface, indicating the presence of unburned surfactant organics. Figs. 8(b)–(d) show the GO/SBA-15 samples at calcination temperatures of 450°C–650°C. The surface morphology of these samples was relatively glossy. This observation indicated that the surfactant organics had been removed. A similar morphology was observed in a previous study [41]. Fig. 8(e) shows the surface morphology of GO/SBA-15 obtained at a calcination temperature of 750°C. Some of the particles aggregated in a compact manner, indicating a decrease in the sample's surface area.

Typical TEM images of GO/SBA-15 particles are displayed in Fig. 9. As observable in Fig. 9(a), the GO/SBA-15 nanoparticles presented porous tissue and were well dispersed. Figs. 9(b) and (c) show a well-ordered array of mesopores with uniform pore size on the (100) crystal face and a uniform tissue of parallel channels on the (110) crystal face. The GO/SBA-15 sample observed in Fig. 9(c) shows a large-scale hexagonal mesostructure (>300 nm). The self-assembly

of silicate species and surfactant micelles constructed this hexagonal mesostructure. The GO/SBA-15 material had a mesopore size of 6.89 nm, which is consistent with the pore size of 6.50 nm calculated through  $N_2$ -adsorption measurement (Fig. 5(b)). Fig. 9(d) shows that the wrinkled GO layer was homogeneously coated on the surface of the porous SBA-15. The sheet-like GO flakes possessed a large surface area and high adsorption capacity.

### 3.5. Adsorption isotherm experiments

Adsorption isotherms were used to investigate the interaction between the MB and the surface of the GO/SBA-15. The experiment was conducted in an MB solution with various concentrations (10–50  $\text{mg L}^{-1}$ ). A certain dosage (10 mg) of the GO/SBA-15 was added to a flask containing 50 mL of MB solution. The suspensions were shaken for 24 h to achieve adsorption equilibrium.

The Langmuir and Freundlich isotherm models were used to evaluate the adsorption data. The Langmuir isotherm equation in linearized form is given as follows:

$$\frac{1}{q_e} = \frac{1}{q_L} + \frac{1}{q_L K_L C_e} \quad (2)$$

where  $C_e$  ( $\text{mg L}^{-1}$ ) is the equilibrium concentration of MB,  $q_e$  ( $\text{mg g}^{-1}$ ) is the adsorption capacity,  $q_L$  ( $\text{mg g}^{-1}$ ) refers to the maximum adsorption capacity, and  $K_L$  ( $\text{mL mg}^{-1}$ ) is the Langmuir constant.

The Freundlich isotherm model in linearized form is expressed by the following equation:

$$\log q_e = \log K_F + \frac{1}{n} \log C_e \quad (3)$$

where  $K_F$  and  $n$  are Freundlich constants.

Fig. 10 shows the isotherms obtained by applying the Langmuir (Fig. 10(a)) and Freundlich (Fig. 10(b)) models to the adsorption data. The most appropriate model was selected by determining the correlation coefficient ( $R^2$ ). As summarized in Table 3, the Langmuir isotherm model had a higher  $R^2$  value, which more accurately fitted the experimental data than that of the Freundlich isotherm model. This suggests that homogeneous distribution of active sites on the adsorbent surface occurs during the adsorption process. This type of adsorption is monolayer adsorption of MB onto the GO/SBA-15 surface with no interaction between adsorbed molecules [34]. Furthermore, the separation factor ( $R_L$ ) falls in the range between 0 and 1, implying that the adsorption process is more likely to occur [42].

### 3.6. Adsorption kinetics experiments

To understand the adsorption behavior, such as adsorption type and rate, of MB onto GO/SBA-15 composites, kinetic models were used to evaluate the adsorption data. In our study, the pseudo-first order, pseudo-second order kinetic model, and intraparticle diffusion model were applied to fit the adsorption kinetic data. The three kinetic models, respectively, are expressed as follows:

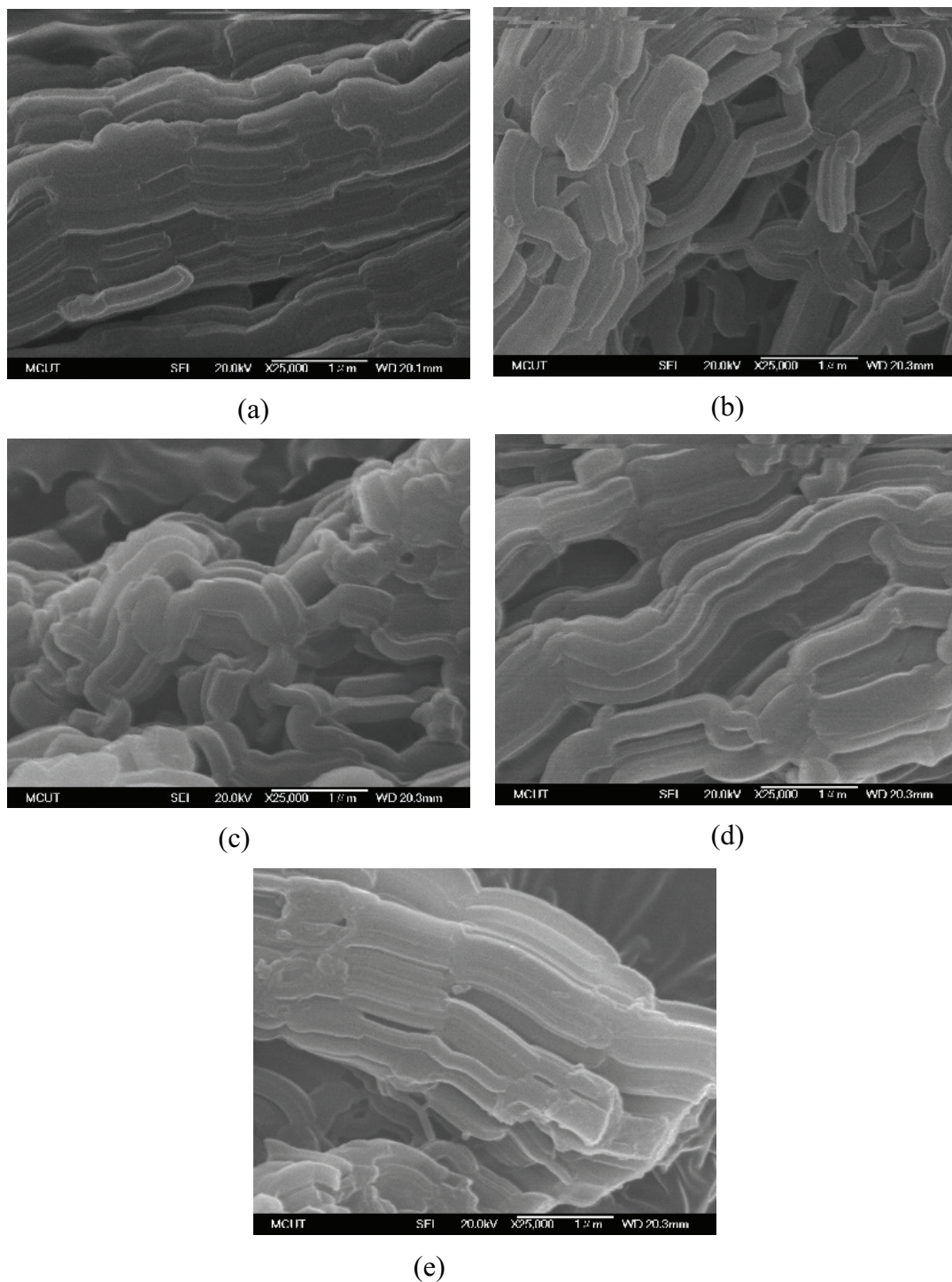


Fig. 8. FE-SEM images of GO/SBA-15 samples at various calcination temperatures: (a) 350°C, (b) 450°C, (c) 550°C, (d) 650°C, (e) 750°C.

$$q_t = q_e(1 - e^{-k_1 t}) \quad (4)$$

$$\frac{t}{q_t} = \frac{1}{k_2 q_e^2} + \frac{t}{q_e} \quad (5)$$

$$q_t = k_i t^{0.5} + I \quad (6)$$

where  $q_e$  ( $\text{mg g}^{-1}$ ) and  $q_t$  ( $\text{mg g}^{-1}$ ) are the adsorption capacity at equilibrium and at time  $t$ ,  $k_1$  and  $k_2$  are the rate constants of adsorption kinetic models,  $k_i$  is an intraparticle diffusion rate constant, and  $I$  is related to the thickness of the boundary.

Fig. 11 indicates the plots of adsorption kinetics after application of the pseudo-first order (Fig. 11(a)) and pseudo-second order (Fig. 11(b)) models. Table 4 demonstrates

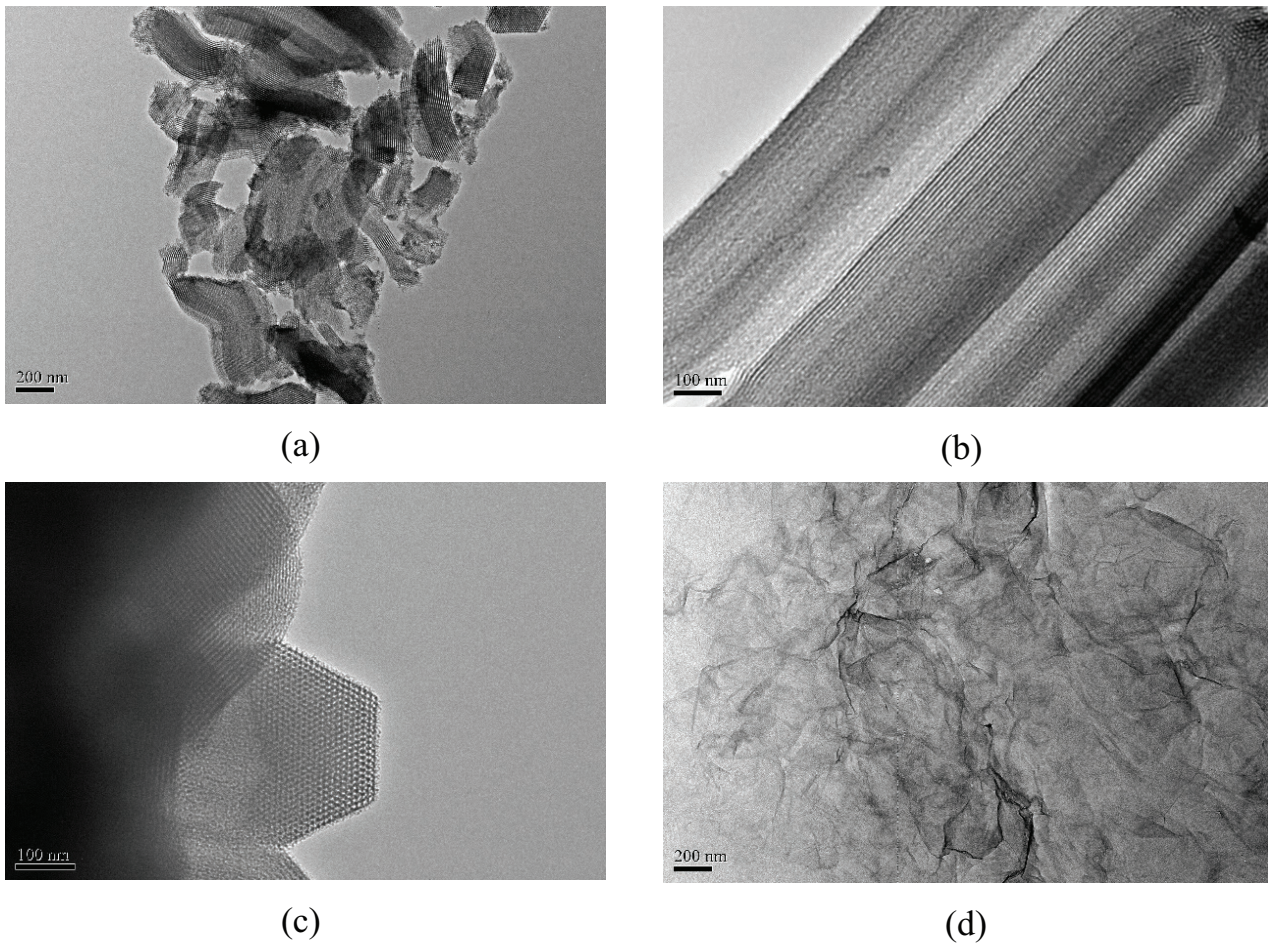


Fig. 9. TEM images of samples: (a)–(c) GO/SBA-15; (d) pure GO.

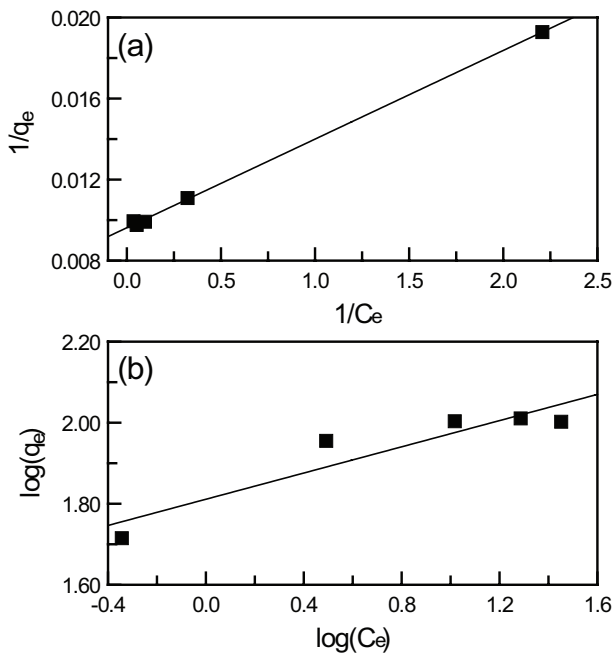


Fig. 10. Adsorption isotherms of MB onto GO/SBA-15: (a) Langmuir model, (b) Freundlich model.

Table 3  
Isotherm parameters for MB adsorption onto GO/SBA-15

Langmuir				Freundlich		
$R_L$	$q_L$ (mg g <sup>-1</sup> )	$K_L$	$R^2$	$n$	$K_F$ (mg g <sup>-1</sup> )	$R^2$
0.0386	102.04	2.2791	0.9989	6.52	64.93	0.8210

that the pseudo-second order model exhibited a higher  $R^2$  value than that of the pseudo-first order model; this observation indicates that the adsorption data were more accurately fitted to the pseudo-second order kinetic model.

Furthermore, the intraparticle diffusion kinetic model was applied to evaluate the diffusion mechanism. The plot of  $q_t$  vs.  $t^{1/2}$  in Fig. 12 shows multilinearity characterization over the whole time range, indicating that three steps occurred in the adsorption process. The intraparticle diffusion rate constants followed a descending trend with increasing adsorption time (Table 4). At the first stage, the diffusion of MB molecules passed the external surface of the GO/SBA-15. The larger  $k_i$  value in the first stage indicates that the removal rate of MB was higher because of the instantaneous availability of a large surface area and active adsorption sites [43]. Subsequently, adsorption saturation was reached on the exterior surface leading to the intra-particle diffusion and

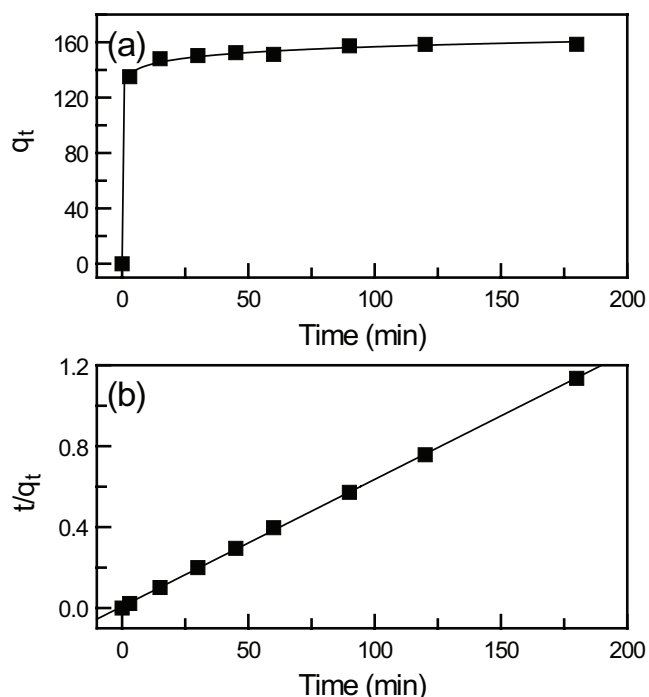


Fig. 11. Adsorption kinetics of MB onto GO/SBA-15: (a) pseudo-first order model, (b) pseudo-second order model.

Table 4  
Kinetics parameters for MB adsorption onto GO/SBA-15

Model	Parameter	Value
Pseudo-First-order adsorption kinetic	$k_1$ ( $\text{min}^{-1}$ )	0.7022
	$q_{e,\text{calculated}}$ ( $\text{mg g}^{-1}$ )	153.83
	$R^2$	0.9940
Pseudo-second-order adsorption kinetic	$k_2$ ( $\text{min}^{-1}$ )	0.0038
	$q_{e,\text{calculated}}$ ( $\text{mg g}^{-1}$ )	159.74
	$R^2$	0.9998
Intraparticle diffusion kinetic	$k_{i1}$ ( $\text{mg g}^{-1} \text{min}^{1/2}$ )	78.0123
	$k_{i2}$ ( $\text{mg g}^{-1} \text{min}^{1/2}$ )	3.4232
	$k_{i3}$ ( $\text{mg g}^{-1} \text{min}^{1/2}$ )	1.1410

diffusion of MB molecules into the pores of the GO/SBA-15. The lower  $k_i$  values in the second and third stages resulted from the long duration of molecule diffusion in the pores of the GO/SBA-15, thus reducing the removal rate of MB. This observation was in good agreement with the results of a previous study on adsorption of diazo dye [44].

### 3.7. Reutilization experiments

Reutilization experiments were carried out to investigate the stability and regeneration ability of the GO/SBA-15 materials. Ethanol was used as a desorption agent that can weaken the ionic interactions between the GO/SBA-15 and MB [45]. Fig. 13 shows the results of adsorption-desorption experiments. The adsorption capacity still remained above 95% after five-time reused, demonstrating the excellent regeneration of the GO/SBA-15 materials.

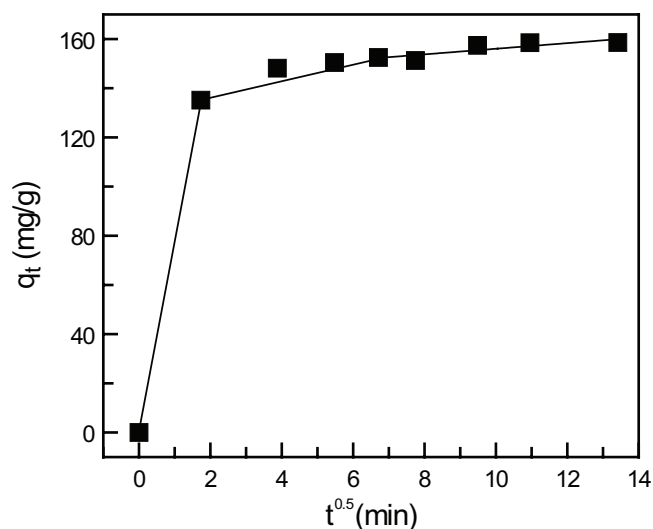


Fig. 12. Intraparticle diffusion plot for MB adsorption onto GO/SBA-15.

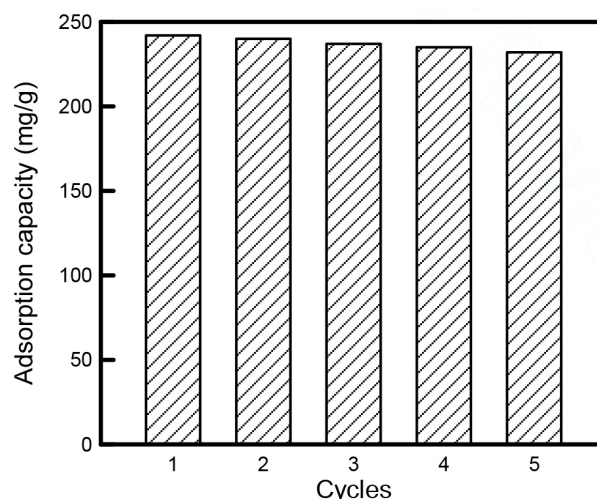


Fig. 13. Reutilization of GO/SBA-15 for MB adsorption in five cycles.

## 4 Conclusions

In this study, mesoporous GO/SBA-15 nanocomposites were successfully synthesized by adding GO into SBA-15. Various experimental parameters including the initial concentration of dye, calcination temperature, and pH of the solution were investigated. Immersion of GO into mesoporous SBA-15 increased MB adsorption capacity. Increasing the initial concentration and solution pH enhanced the adsorption efficiency of GO/SBA-15. Optimal MB adsorption was observed at a calcination temperature of 550°C.  $\text{N}_2$  adsorption-desorption measurement indicated that the GO/SBA-15 samples were mesoporous materials with uniform pore distribution. The addition of GO did not affect the mesostructure of the SBA-15 framework. The GO/SBA-15 possessed a large surface area of  $891 \text{ m}^2 \text{ g}^{-1}$ , large pore volume of  $1.035 \text{ cm}^3 \text{ g}^{-1}$ , and wide pore diameter of 6.50 nm. TEM of the synthesized GO/SBA-15 revealed that GO was

homogeneously coated on the surface of mesoporous SBA-15. The adsorption isotherm and kinetics were more closely represented by the Langmuir model and pseudo-second order model, respectively, indicating that the adsorption type was monolayer adsorption. This method of preparing GO/SBA-15 composite is potentially useful for removing organic pollutants from wastewater.

## Symbols

$C_o$	–	Initial MB concentration, mg L <sup>-1</sup>
$C_t$	–	MB concentration at different adsorption times, mg L <sup>-1</sup>
$I$	–	Thickness of the boundary, m
$k_1$	–	Rate constants of pseudo-first order kinetic models, min <sup>-1</sup>
$k_2$	–	Rate constants of pseudo-second order kinetic model, min <sup>-1</sup>
$k_i$	–	Intraparticle diffusion rate constant, mg g <sup>-1</sup> min <sup>1/2</sup>
$q_e$	–	Amount of MB adsorbed onto the GO/SBA-15 at equilibrium, mg g <sup>-1</sup>
$q_t$	–	Amount of MB adsorbed onto the GO/SBA-15 at time t, mg g <sup>-1</sup>
$V$	–	Volume of the MB solution, mL
$W$	–	Weight of the GO/SBA-15, g

## Acknowledgments

The author expresses thanks to the Ministry of Science and Technology (MOST) as well as Ming Chi University of Technology (MCUT) of Taiwan for their financial supports under Project No. MOST 106–2221–E–131–029 and VL006-1300-108.

## References

- [1] P.K. Sandhya, J. Jose, M.S. Sreekala, M. Padmanabhan, N. Kalarikkal, S. Thomas, Reduced graphene oxide and ZnO decorated graphene for biomedical applications, *Ceram. Int.*, 44 (2018) 15092–15098.
- [2] M. Mesallam, E. Sheha, E.M. Kamar, N. Sharma, Graphene and magnesiated graphene as electrodes for magnesium ion batteries, *Mater. Lett.*, 232 (2018) 103–106.
- [3] Y. Peng, D. Lin, J.J. Gooding, Y. Xue, L. Dai, Flexible fiber-shaped non-enzymatic sensors with a graphene-metal heterostructure based on graphene fibres decorated with gold nanosheets, *Carbon*, 136 (2018) 329–336.
- [4] S. Meti, M.R. Rahman, M.I. Ahmad, K.U. Bhat, Chemical free synthesis of graphene oxide in the preparation of reduced graphene oxide-zinc oxide nanocomposite with improved photocatalytic properties, *Appl. Surf. Sci.*, 451 (2018) 67–75.
- [5] D.G. Papageorgiou, I.A. Kinloch, R.J. Young, Mechanical properties of graphene and graphene-based nanocomposites, *Prog. Mater. Sci.*, 90 (2017) 75–12.
- [6] X. Li, Y. Tang, J. Song, W. Yang, M. Wang, C. Zhu, W. Zhao, J. Zheng, Y. Lin, Self-supporting activated carbon/carbon nanotube/reduced graphene oxide flexible electrode for high performance supercapacitor, *Carbon*, 129 (2018) 236–244.
- [7] R. Sitko, B. Zawisza, E. Talik, P. Janik, G. Osoba, B. Feist, E. Malicka, Spherical silica particles decorated with graphene oxide nanosheets as a new sorbent in inorganic trace analysis, *Anal. Chim. Acta*, 834 (2014) 22–29.
- [8] M. Khazaei, S. Nasser, M.R. Ganjali, M. Khoobi, R. Nabizadeh, A.H. Mahvi, E. Gholibegloo, S. Nazmara, Modeling mercury (II) removal at ultra-low levels from aqueous solution using graphene oxide functionalized with magnetic nanoparticles: optimization, kinetics, and isotherm studies, *Desal. Wat. Treat.*, 83 (2017) 144–158.
- [9] A. Azizi, A. Torabian, E. Moniri, A.H. Hassani, H.A. Panahi, Novel synthesis of graphene oxide with polystyrene for the adsorption of toluene, ethylbenzene and xylenes from wastewater, *Desal. Wat. Treat.*, 74 (2017) 248–257.
- [10] Z.L. Wu, F. Liu, C.K. Li, X.Q. Chen, J.G. Yu, A sandwich-structured graphene-based composite: preparation, characterization, and its adsorption behaviors for Congo red, *Colloid Surf. A*, 509 (2016) 65–72.
- [11] B.Y. Yue, L.Y. Yu, F.P. Jiao, X.Y. Jiang, J.G. Yu, The fabrication of pentaerythritol pillared graphene oxide composite and its adsorption performance towards metal ions from aqueous solutions, *Desal. Wat. Treat.*, 102 (2018) 124–133.
- [12] X. Hu, Y. Yu, W. Hou, J. Zhou, L. Song, Effects of particle size and pH value on the hydrophilicity of graphene oxide, *Appl. Surf. Sci.*, 273 (2013) 118–121.
- [13] Z.L. Cheng, Y.X. Li, Z. Liu, Novel adsorption materials based on graphene oxide/Beta zeolite composite materials and their adsorption performance for rhodamine B, *J. Alloys. Compd.*, 708 (2017) 255–263.
- [14] X.L. Wu, Y. Shi, S. Zhong, H. Lin, J.R. Chen, Facile synthesis of Fe<sub>3</sub>O<sub>4</sub>-graphene@mesoporous SiO<sub>2</sub> nanocomposites for efficient removal of Methylene Blue, *Appl. Surf. Sci.*, 378 (2016) 80–86.
- [15] F.J. Martín-Jimeno, F. Suárez-García, J.I. Paredes, A. Martínez-Alonso, J.M.D. Tascón, Activated carbon xerogels with a cellular morphology derived from hydrothermally carbonized glucose-graphene oxide hybrids and their performance towards CO<sub>2</sub> and dye adsorption, *Carbon*, 81 (2015) 137–147.
- [16] M.O. Ansari, R. Kumar, S.A. Ansari, S.P. Ansari, M.A. Barakat, A. Alshahrie, M.H. Cho, Anion selective pTSA doped polyaniline@graphene oxide-multiwalled carbon nanotube composite for Cr(VI) and Congo red adsorption, *J. Colloid Interface Sci.*, 496 (2017) 407–415.
- [17] J.Y. Yang, X.Y. Jiang, F.P. Jiao, J.G. Yu, The oxygen-rich pentaerythritol modified multi-walled carbon nanotube as an efficient adsorbent for aqueous removal of alizarin yellow R and alizarin red S, *Appl. Surf. Sci.*, 436 (2018) 198–206.
- [18] G. Zhou, K.P. Wang, H.W. Liu, L. Wang, X.F. Xiao, D.D. Dou, Y.B. Fan, Three-dimensional polylactic acid@graphene oxide/chitosan sponge bionic filter: Highly efficient adsorption of crystal violet dye, *Int. J. Biol. Macromol.*, 113 (2018) 792–803.
- [19] X. Xu, J. Zou, J. Teng, Q. Liu, X.Y. Jiang, F.P. Jiao, J.G. Yu, X.Q. Chen, Novel high-gluten flour physically cross-linked graphene oxide composites: hydrothermal fabrication and adsorption properties for rare earth ions, *Ecotoxicol. Environ. Saf.*, 166 (2018) 1–10.
- [20] X. Xu, X.Y. Jiang, F.P. Jiao, X.Q. Chen, J.G. Yu, Tunable assembly of porous three-dimensional graphene oxide-corn zein composites with strong mechanical properties for adsorption of rare earth elements, *J. Taiwan Inst. Chem. Eng.*, 85 (2018) 106–114.
- [21] S. Singh, R. Kumar, H.D. Setiabudi, S. Nanda, D.V.N. Vo, Advanced synthesis strategies of mesoporous SBA-15 supported catalysts for catalytic reforming applications: a state-of-the-art review, *Appl. Catal., A*, 559 (2018) 57–74.
- [22] H. Fida, G. Zhang, S. Guo, A. Naeem, Heterogeneous Fenton degradation of organic dyes in batch and fixed bed using La-Fe montmorillonite as catalyst, *J. Colloid Interface Sci.*, 490 (2017) 859–868.
- [23] T.H. Liou, L.W. Hung, C.L. Liu, T.Y. Zhang, Direct synthesis of nano titania on highly-ordered mesoporous SBA-15 framework for enhancing adsorption and photocatalytic activity, *J. Porous Mater.*, 25 (2018) 1337–1347.
- [24] Q. Du, J. Sun, Y. Li, X. Yang, X. Wang, Z. Wang, L. Xia, Highly enhanced adsorption of congo red onto graphene oxide/chitosan fibers by wet-chemical etching off silica nanoparticles, *Chem. Eng. J.*, 245 (2014) 99–106.
- [25] C. Santhosh, V. Velmurugan, G. Jacob, S.K. Jeong, A.N. Grace, A. Bhatnaga, Role of nanomaterials in water treatment applications: A review, *Chem. Eng. J.*, 306 (2016) 1116–1137.
- [26] J.G. Yu, J. Zou, L.L. Liu, X.Y. Jiang, F.P. Jiao, X.Q. Chen, Preparation of TiO<sub>2</sub>-based photocatalysts and their

- photocatalytic degradation properties for methylene blue, rhodamine B and methyl orange, *Desal. Wat. Treat.*, 81 (2017) 282–290.
- [27] V.W.O. Wanjeri, C.J. Sheppard, A.R.E. Prinsloo, J.C. Ngila, P.G. Ndungu, Isotherm and kinetic investigations on the adsorption of organophosphorus pesticides on graphene oxide based silica coated magnetic nanoparticles functionalized with 2-phenylethylamine, *J. Environ. Chem. Eng.*, 6 (2018) 1333–1346.
- [28] X. Wang, M. Lu, H. Wang, Y. Pei, H. Rao, X. Du, Three-dimensional graphene aerogels–mesoporous silica frameworks for superior adsorption capability of phenols, *Sep. Purif. Technol.*, 153 (2015) 7–13.
- [29] W.S. Hummers Jr., R.E. Offeman, Preparation of graphitic oxide, *J. Am. Chem. Soc.*, 80 (1958) 1339–1339.
- [30] X. Li, Z. Wang, Q. Li, J. Ma, M. Zhu, Preparation, characterization, and application of mesoporous silica-grafted graphene oxide for highly selective lead adsorption, *Chem. Eng. J.*, 273 (2015) 630–637.
- [31] E.P. Barrett, L.G. Joyner, P.P. Halenda, The determination of pore volume and area distributions in porous substances. I. Computations from nitrogen isotherms, *J. Am. Chem. Soc.*, 73 (1951) 373–380.
- [32] F. Liu, Z. Wu, D. Wang, J. Yu, X. Jiang, X. Chen, Magnetic porous silica–graphene oxide hybrid composite as a potential adsorbent for aqueous removal of p-nitrophenol, *Colloid Surf. A.*, 490 (2016) 207–214.
- [33] R. Sabarish, G. Unnikrishnan, Polyvinyl alcohol/carboxymethyl cellulose/ZSM-5 zeolite biocomposite membranes for dye adsorption applications, *Carbohydr. Polym.*, 199 (2018) 129–140.
- [34] M.R. Malekbala, M. AliKhan, S. Hosseini, L.C. Abdullah, T.S.Y. Choong, Adsorption/desorption of cationic dye on surfactant modified mesoporous carbon coated monolith: equilibrium, kinetic and thermodynamic studies, *J. Ind. Eng. Chem.*, 21 (2015) 369–377.
- [35] T.H. Liou, J.Y. Jheng, Synthesis of high-quality ordered mesoporous carbons using a sustainable way from recycling of e-waste as a silica template source, *ACS Sustainable Chem. Eng.*, 6 (2018) 6507–6517.
- [36] T.H. Liou, A green route to preparation of MCM-41 silicas with well-ordered mesostructure controlled in acidic and alkaline environments, *Chem. Eng. J.*, 171 (2011) 1458–1468.
- [37] K.S. Lakhi, G. Singh, S. Kim, A.V. Baskar, S. Joseph, J.H. Yang, H. Ilbeygi, S.J.M. Ruban, V.T.H. Vu, A. Vinu, Mesoporous Cu-SBA-15 with highly ordered porous structure and its excellent CO<sub>2</sub> adsorption capacity, *Microporous Mesoporous Mat.*, 267 (2018) 134–141.
- [38] W. Peng, H. Li, Y. Hu, Y. Liu, S. Song, Characterisation of reduced graphene oxides prepared from natural flaky, lump and amorphous graphites, *Mater. Res. Bull.*, 78 (2016) 119–127.
- [39] B. Szczeńśniak, J. Choma, M. Jaroniec, Effect of graphene oxide on the adsorption properties of ordered mesoporous carbons toward H<sub>2</sub>, C<sub>6</sub>H<sub>6</sub>, CH<sub>4</sub> and CO<sub>2</sub>, *Microporous Mesoporous Mat.*, 261 (2018) 105–110.
- [40] N. Saeidi, M. Parvini, Z. Niavarani, High surface area and mesoporous graphene/activated carbon composite for adsorption of Pb(II) from wastewater, *J. Environ. Chem. Eng.*, 3 (2015) 2697–2706.
- [41] J. Wang, H. Ge, W. Bao, Synthesis and characteristics of SBA-15 with thick pore wall and high hydrothermal stability, *Mater. Lett.*, 145 (2015) 312–315.
- [42] X. Wang, C. Jiang, B. Hou, Y. Wang, C. Hao, J. Wu, Carbon composite lignin-based adsorbents for the adsorption of dyes, *Chemosphere*, 206 (2018) 587–596.
- [43] Y. Li, Q. Du, T. Liu, J. Sun, Y. Wang, S. Wu, Z. Wang, Y. Xia, L. Xia, Methylene blue adsorption on graphene oxide/calcium alginate composites, *Carbohydr. Polym.*, 95 (2013) 501–507.
- [44] M. Toor, B. Jin, Adsorption characteristics, isotherm, kinetics, and diffusion of modified natural bentonite for removing diazo dye, *Chem. Eng. J.*, 187 (2012) 79–88.
- [45] M. Yang, X. Liu, Y. Qi, W. Sun, Y. Men, Preparation of κ-carrageenan/graphene oxide gel beads and their efficient adsorption for methylene blue, *J. Colloid Interface Sci.*, 506 (2017) 669–677.